JGR Oceans

Key Points:

- We characterize the response of ocean skin temperature to rain using in situ observations of 69 rain events
- Skin temperature depresses in response to rain at all wind speeds, and the skin-bulk temperature difference levels off in intense rain
- We test a prognostic model for the influence of rain on ocean skin temperature and demonstrate a realistic modification to improve it

The Response of Ocean Skin Temperature to Rain: Observations and Implications for Parameterization of Rain-Induced Fluxes

Carson R. Witte[1] [iD] **, Christopher J. Zappa[1]** [iD] **, and James B. Edson[2]** [iD]

[1]Lamont-Doherty Earth Observatory, Columbia University, Palisades, NY, USA, [2]Woods Hole Oceanographic Institution, Woods Hole, MA, USA

Abstract Rainfall alters the physical and chemical properties of the surface ocean, and its effect on ocean skin temperature and surface heat fluxes is poorly represented in many air-sea interaction models. We present radiometric observations of ocean skin temperature, near-surface (5 cm) temperature from a towed thermistor, and bulk atmospheric and oceanic variables, for 69 rain events observed over the course of 4 months in the Indian Ocean as part of the DYNAMO project. We test a state-of-the-art prognostic model developed by Bellenger et al. (2017, https://doi.org/10.1002/2016JC012429) to predict ocean skin temperature in the presence of rain, and demonstrate a physically motivated modification to the model that improves its performance with increasing rain rate. We characterize the vertical skin-bulk temperature gradient induced by rain and find that it levels off at high rain rates, suggestive of a transition in skin-layer physics that has been previously hypothesized in the literature. We also quantify the small bias that will be present in turbulent sensible heat fluxes parameterized from ocean temperature measurements made at typical "bulk" depths during a rain event. Finally, a wind threshold is observed above which the surface ocean remains well-mixed during a rain event; however, the skin temperature is observed to decrease at all wind speeds in the presence of rain.

Plain Language Summary We measured the change in ocean surface temperature throughout 69 rain events over the course of 4 months in the Indian Ocean, and used these measurements to improve a model of how the surface ocean temperature changes with rainfall. We also found that rain lowers the temperature of the ocean's skin even in the presence of high winds, and that the difference between the ocean skin temperature and the temperature of water 5 m deep approaches a constant value at high rain rates.

1. Introduction

The ocean surface is typically characterized by a thermal "skin layer" less than a millimeter thick through which molecular conduction is the primary method of heat transfer (Ewing & McAlister, 1960). The sum of net long-wave radiation and turbulent heat fluxes at the air-sea interface is generally negative (heat flow out of the ocean), resulting in a temperature gradient across the thermal skin layer with an interface temperature that is cooler than the base of the layer by 0.1°C–0.5°C (Fairall, Bradley, Godfrey, et al., 1996). This temperature difference across the skin layer can constitute a significant portion of the total air-sea temperature difference (or even change its sign), and thus accurate specification of the interface temperature is critical to estimation of air-sea heat fluxes (Fairall, Bradley, Rogers, et al., 1996; Saunders, 1967). While the true air-sea interfacial temperature T_{int} is a hypothetical quantity we cannot measure directly (Donlon et al., 2007), we instead measure the closely-related "skin temperature" T_{skin} at a depth of 10–20 µm using an infrared radiometer operating at wavelengths of 3.7–12 µm (Katsaros, 1980). The temperature at the base of the thermal skin layer is denoted $T_{subskin}$, while temperature at a specific depth z is denoted T_z following Donlon et al. (2007). These distinctions, combined with physical understanding of the processes that drive variability at each depth, are critical for interpretation and inter-comparison of satellite and in situ measurements of the "Sea Surface Temperature" (SST) and resulting estimates of air-sea heat flux.

Precipitation disturbs the thermal skin through multiple processes (discussed in detail in Section 1.1), which change the relationship between T_{skin} and the temperature of underlying waters (Godfrey et al., 1999). Rain cells display high levels of spatiotemporal heterogeneity—at scales well below the footprint of current infrared and microwave satellite temperature sensors—and consequently rainfall will generate horizontal SST gradients that have been shown to impact atmospheric convection and boundary-layer circulation, and even initiate further

precipitation (de Szoeke et al., 2014; Li & Carbone, 2012; Reverdin et al., 2020; Soloviev & Lukas, 1996). Quantitative understanding of the physical relationship between rain and skin temperature is therefore critical to studies of atmospheric circulation patterns and prediction of global weather and climate, as well as interpretation of satellite remote sensing measurements.

### 1.1. During the Storm: Local Impact of Rain on the Thermal Skin

For a given rain rate, expressed in terms of vertical accumulation of water per time (e.g., mm/hr), there is a characteristic distribution of raindrop sizes ranging from about 0.1—5 mm in diameter (Marshall & Palmer, 1948). Most raindrops that impact the ocean are traveling at their terminal velocity, and drops smaller than a critical radius of about 0.4 mm (with correspondingly lower impact velocities) will be unable to break the surface tension and will accumulate in the skin layer (Oğuz & Prosperetti, 1991; Schlüssel et al., 1997). Larger raindrops falling at faster terminal velocities will penetrate the skin, each creating an impact crater that rebounds into an upward jet, generating outward-propagating ring waves (Engel, 1966; Morton et al., 2000; Prosperetti & Oguz, 1993). Secondary drops will break off from the rebounding jets, a few of which (depending on their size) are likely carried aloft by turbulence (Edson & Fairall, 1994; Mueller & Veron, 2014; Veron, 2015). At sufficiently high rain rates, the interface becomes completely disturbed by violent surface motions as impact craters and splashing droplets interact continuously with impinging raindrops, and the ring wave patterns are lost (Laxague & Zappa, 2020; Peirson et al., 2013).

The thermal skin layer is known to reform rapidly after being disturbed by processes such as wave breaking, with a characteristic timescale of a few seconds (Ewing & McAlister, 1960; Jessup et al., 1997). The kinetic energy of penetrating raindrops is comparable in magnitude to breaking waves, and the impact craters they create are generally deeper than the skin layer (Engel, 1966; Zappa et al., 2009). This leads to additional surface renewals with increasing rain rate, and in all but the lightest of rains (<2 mm/hr) the surface renewal timescale is dominated by the precipitation effect (Craeye & Schlüssel, 1998; Schlüssel et al., 1997). Enhanced centimeter-scale surface roughness caused by the rainfall increases tangential stress while damping wind-wave growth, changing the nature of the air-sea momentum flux such that a greater fraction of wind energy goes into acceleration of the near-surface current rather than wave growth (Houk & Green, 1976; Laxague & Zappa, 2020; Poon et al., 1992; Schlüssel et al., 1997).

Mixing a volume of rainwater into the surface ocean results in a sensible heat flux driven by the temperature difference between the ocean and the raindrops (Gosnell et al., 1995; Schlüssel et al., 1997). Because the raindrops must be at or below the atmospheric wet bulb temperature, they will cool the ocean surface in the vast majority of cases (e.g., Dong et al., 2017; Flament & Sawyer, 1995; Reverdin et al., 2012; Volkov et al., 2019). Modeling and observations have confirmed that raindrops are generally within 0.2°C of the wet bulb temperature (Anderson et al., 1998; Gosnell et al., 1995). The "rain sensible heat flux" can be quite significant both while it is raining (when it can be well over 50% of the net surface heat flux) as well as on monthly timescales in regions of high precipitation, where it has been observed to account for 2%–15% of the longer-term heat flux (Anderson et al., 1998; Fairall, Bradley, Godfrey, et al., 1996). Raindrops that do not penetrate the skin are a heat flux to the skin layer itself, while penetrating drops form a volume source in the upper tens of centimeters. However, because this volume source is also driving increased turbulent surface renewals, skin temperature is influenced by a combination of both processes (Schlüssel et al., 1997; Soloviev & Schlüssel, 1996).

While the cooler temperature of the rain is a significant source of sensible heat flux, the buoyancy flux is dominated by rain's freshening effect, which is around 15 times greater than the negative buoyancy produced by rain cooling (Thompson et al., 2019). The remnants of raindrops that have penetrated to depth are thus expected to rise back toward the surface once their kinetic energy has dissipated, a buoyancy effect that stands in addition to the increase in turbulent surface renewals caused by their initial impacts. Rain can produce buoyancy fluxes that are more than an order of magnitude larger than typically produced by surface heating—a 10 mm/hr rain rate produces the equivalent of an 850 W/m^2 net surface heat flux (Thompson et al., 2019). Given that typical nighttime surface cooling is on the order of 400 W/m^2, rainfall can thus stabilize nocturnal ocean convection (Thompson et al., 2019).

Figure 1 displays the evolution of ocean surface slope and skin temperature over the course of a rain event observed in October 2016 in the Timor Sea (Wurl et al., 2018). Along-look surface slope was measured by an

Ocean Surface Slope and Temperature through Rain Event
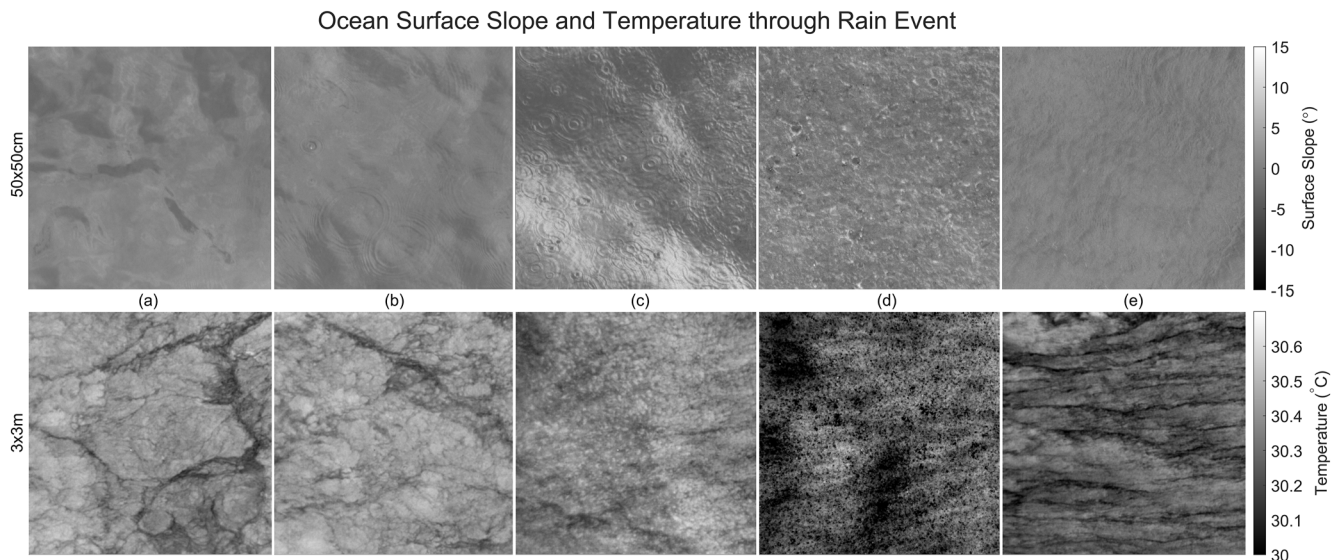
Figure 1. Polarimetric (top) and Infrared (bottom) imagery of a rain event observed on 20 October 2016 onboard R/V Falkor in the Timor Sea, showing (a) conditions prior to rain onset, (b) light rain, (c) heavy rain, (d) extreme rain, and (e) after rain.

imaging polarimeter (Laxague & Zappa, 2020; Zappa et al., 2008), while skin temperature was measured by a cooled infrared camera processed through a 5-frame median filter to remove falling raindrops from the images. Light rain (panel b) generates a few ring waves but has little effect on the thermal structure of the ocean skin. As the intensity of the rain increases and a larger number of raindrops penetrate the ocean surface (panel c), they disturb the cool skin and enhance mixing in the very-near-surface layer, generating additional surface renewals and leading to localized increases in skin temperature as warmer subskin water is brought to the surface. However, the overall temperatures of both skin and subskin water are decreasing throughout the event because the raindrops are colder than the ocean. In very intense rain (panel d, with a rain rate above 100 mm/hr), the surface becomes a chaotic world of impact craters and splashes, and the ability of the infrared sensor to see the surface may be impeded by raindrops in the optical path. After the rain event (panel e), skin temperature is colder, and the larger-scale convective features characteristic of the pre-rain ocean surface have been replaced by streaks reminiscent of wind-driven Langmuir circulation.

1.2. After the Storm: Rain Layers

In winds of less than about 10 m/s, the strength of the buoyancy flux associated with rainfall leads to the development of a stable, low-salinity layer on the ocean surface, examples of which have been observed with typical horizontal scale of about 10 km and vertical thickness of 1–2 m (Anderson et al., 1996; Asher et al., 2014; Cronin & McPhaden, 1999; Smyth et al., 1996b; Soloviev & Lukas, 1997b; Thompson et al., 2019; Wijesekera et al., 1999, 2003; Wijesekera & Gregg, 1996; You, 1995). The buoyancy stratification effectively isolates the underlying water from wind forcing, leading to a reduction in turbulent dissipation by two orders of magnitude across the bottom of the layer (Smyth et al., 1997; ten Doeschate et al., 2019; Wijesekera et al., 2003; Zappa et al., 2009). These isolated layers (which can also be formed by diurnal heating) become "slippery," responding to wind forcing by flowing over the underlying water with very little friction (Harrison & Veron, 2017; Kudryavtsev & Soloviev, 1990; Shcherbina et al., 2019). Just as the turbulent forcing is trapped in the layer, heat becomes trapped in the layer as well, influencing the diurnal SST cycle (Soloviev & Lukas, 1997a). Observations also suggest that the layer can trap internal waves via resonant interaction with the underlying stratification, which then modulate SST at scales around 100 m (Soloviev & Lukas, 1996; Soloviev et al., 2015).

Rain layers are observed to persist on timescales of a few hours to a day, with wind-driven mixing being the primary control on their destruction (Thompson et al., 2019; Volkov et al., 2019). They are subject to rapid advection as they "slip" along the top of the ocean, and surface salinity depressions uncorrelated with local rain rate are observed regularly in regions of high rainfall, suggesting the passage of freshwater pools left by previous

events (Smyth et al., 1996a; Thompson et al., 2019). The fresher rain lens is lighter (less dense) than the surrounding seawater, so it spreads out on the surface, slowly getting thinner and wider via gravity currents acting along the pressure gradients induced by the density anomaly at the lens edges (Soloviev & Lukas, 1997b; Soloviev et al., 2002, 2015). Because the layer is simultaneously undergoing wind-driven advection, a spatial asymmetry develops in which near-surface convergence and downwelling at the leading (downwind) edge of the lens leads to sharp density fronts, which are often observed in association with freshwater lenses (Soloviev & Lukas, 1997b; Soloviev et al., 2002, 2015; Wijesekera et al., 2003). The trapping of internal waves in the layer may also be a mechanism for generating repeating frontal interfaces (Soloviev et al., 2015). Longer-term mixing of rain layers into the surface ocean is thought to drive the evolution of the salinity-stratified "barrier layer" between the mixed layer and the thermocline that is an intrinsic feature of the western Pacific warm pool (Anderson et al., 1996; Lukas & Lindstrom, 1991; A. Soloviev & Lukas, 1996).

In this paper, we will describe a prognostic model for skin and subskin temperature in the presence of rain developed by Bellenger et al. (2017), and suggest a physically-motivated modification to the model. We will then use data collected during the DYNAMO experiment in the equatorial Indian Ocean to directly investigate the skin temperature response to rainfall and evaluate the consistency between observed and modeled responses.

2. Methods

2.1. Prognostic Model for the Influence of Rain Physics on Skin Temperature

Here we describe a state-of-the-art prognostic model for the evolution of skin and subskin properties in the presence of rain built on work by Zeng and Beljaars (2005) and Takaya et al. (2010) and developed in detail by Bellenger et al. (2017) for both temperature and salinity. We focus here on the temperature formulation, starting from the 1-dimensional heat transfer equation:

$$\frac{\partial T}{\partial t} = \frac{\partial}{\partial z}(K_w + k_w)\frac{\partial T}{\partial z} + \frac{1}{\rho_w c_w}\frac{\partial I_S}{\partial z}$$

(1)

where T is temperature, t is time, z is depth (positive upward), K_w is the turbulent diffusion coefficient, k_w is molecular thermal conductivity, I_S is the net solar shortwave (SW) flux (positive into the ocean), and ρ_w and c_w are density and volumetric heat capacity, respectively (the subscript w refers to "water"). We divide the upper ocean into two vertical segments: within the skin layer, where molecular conduction dominates, and below the skin layer, where turbulent processes dominate.

2.1.1. Within the Thermal Skin Layer

Within the thermal skin layer, we make the following assumptions.

- K_w is negligible (molecular processes dominate)
- $\frac{\partial T}{\partial t}$ is negligible (system is in steady state)
- Boundary condition: $\rho_w c_w k_w \frac{\partial T}{\partial z} = Q$ at $z = 0$, where Q is the net heat flux at the surface.

Applying the boundary condition and integrating Equation 1 with depth yields an expression for the temperature difference across the layer:

$$T_{\text{int}} - T_{\text{subskin}} = \frac{\delta}{\rho_w c_w k_w}(Q + I_S f_S(\delta))$$

(2)

where δ is the thickness of the skin layer, which is a function of the buoyancy flux Q_b and the friction velocity u_{*w} (see Equations 12–14 in Fairall, Bradley, Godfrey, et al., 1996; Saunders, 1967); I_s is the surface SW flux; and $f_s(\delta)$ is the fraction of the SW flux absorbed within the layer (see Equation 5 in Zeng & Beljaars, 2005).

The effects of rain are incorporated into Equation 2 by deriving expressions for the friction velocity and buoyancy flux. Specifically, the mixing due to kinetic energy of the penetrating raindrops, as well as the modification of the tangential stress due to enhanced surface roughness, are both incorporated into calculation of the friction velocity u_{*w}:

$$u_{*w} = \left[\frac{1}{\rho_w}(\tau_{\text{wind}} + (1 - f_V(\delta))\tau_{\text{rain}} + (f_V(0) - f_V(\delta))\tau_k)\right]^{1/2}$$

(3)

where τ_{wind} is the wind stress, τ_{rain} is the additional tangential stress induced by rain, τ_k is a parameterization of the rain-driven mixing, and f_V is the decay function of the freshwater volume due to rain (see Equations 7–10 in Bellenger et al., 2017). Thus $f_V(\delta)$ is the fraction of rain volume that penetrates to <u>at least</u> a depth of δ, and $f_V(0)$ is the fraction of rain penetrating into the ocean (i.e., all drops large enough to break the surface tension).

The sensible heat flux due to rain is incorporated following Gosnell et al. (1995) as an additional term in the net surface heat flux Q, which also contains net longwave (I_L), latent (Q_{Lat}), and sensible (Q_{Sens}) heat fluxes:

$$Q = I_L + Q_{\text{Lat}} + Q_{\text{Sens}} + Q_{\text{Rain}}(1 - f_V(\delta)) \tag{4}$$

$$Q_{\text{Rain}} = -c_w R \Delta T \epsilon \left(1 + B^{-1}\right) \tag{5}$$

where R is the rain rate in mm/hr, ΔT is the air-sea temperature difference, c_w is the specific heat of seawater, ϵ is the wet-bulb factor, and B is the bulk Bowen ratio (see Gosnell et al., 1995 for detailed derivation of ϵ and B). As shown in Equation 4, Bellenger et al. (2017) choose to scale Q_{Rain} by the volume fraction of rain that penetrates only to depths within the thermal skin. However, we posit that this term should not be scaled based on the initial penetration depth of the raindrops, given the enhanced renewal processes being driven by impact craters that are deeper than the skin thickness, as well as the buoyancy forcing that is likely to return drop remnants toward the surface after their initial penetration. For this reason, we will test both the model as formulated by Bellenger et al. (2017) (referred to as "Original") and a modified version where Q_{Rain} is not scaled by the volume fraction of rain used in Equation 4 (referred to as "Modified").

Finally, the competing thermal and haline buoyancy effects of rain are incorporated into calculation of the buoyancy flux Q_b, which differs from the heat flux Q in that it includes the "virtual cooling" due to evaporation and precipitation effects:

$$Q_b = I_L + Q_{\text{Lat}} + Q_{\text{Sens}} + Q_{\text{Rain}}(1 - f_V(\delta)) + \frac{\beta c_w}{\alpha} S \left(\frac{Q_{\text{Lat}}}{L_v} - P(1 - f_V(\delta)) \right) \tag{6}$$

where S is the nominal salinity of the layer, L_v is the latent heat of vapourization, P is precipitation rate expressed as a mass flux per unit area in kg m^{-2} s^{-1}, and α and β are the thermal expansion and haline contraction coefficients, respectively. We raise the same concern here regarding the validity of scaling the rain terms by the fraction of rain volume that initially penetrates only to depths within the skin layer.

2.1.2. Below the Thermal Skin Layer

Below the thermal skin layer, we make the following assumptions.

- k_w is negligible (turbulent processes dominate)
- Boundary condition: $\rho_w c_w K_w \frac{\partial T}{\partial z} = Q + I_S - I(z)$ at $z = -\delta$, where $I(z)$ is the net SW radiation at depth z.

Applying the boundary condition and integrating Equation 1 with depth yields:

$$\frac{\partial}{\partial t} \int T \mathrm{d}z = \frac{Q + I_S - I(-d)}{\rho_w c_w} - K_w \frac{\partial T}{\partial z} \Big|_{z=-d} \tag{7}$$

where d is the "foundation depth" at which the mixed layer temperature remains constant through a precipitation event (taken to be 3 m). An idealized profile of $\partial T/\partial z$ and a parameterization for K_w are assumed (see Equations 11–12 in Bellenger et al., 2017) to yield a final differential equation for the temperature change across the subskin layer:

$$\frac{\partial}{\partial t}(T_{-\delta} - T_{-d}) = \frac{Q + I_S - I(-d)}{d \rho_w c_w \eta/(\eta+1)} - \frac{(\eta+1)\kappa u_{*w}}{d \phi_t \left(\frac{d}{L}\right)}(T_{-\delta} - T_{-d}) \tag{8}$$

where $\kappa = 0.4$ is the Von Karman constant, η is an empirical parameter from the idealized temperature profile that includes a wind-speed dependence (see Section 2.2 in Bellenger et al., 2017), ϕ_t is the non-dimensional temperature gradient function from Monin-Obukhov similarity theory (see Equation 5 in Takaya et al., 2010) and L is the Monin-Obhukov length (see Equations 13–15 in Bellenger et al., 2017). The rain-induced surface stress term τ_{rain} is included without scaling in the calculation of u_{*w} for the subsurface layer, but the turbulent mixing

by raindrops τ_k is neglected. A lateral spreading term is also introduced, which is critical for studies of rain layer persistence and evolution but has relatively little effect on the model at our observational timescales.

This model, as derived in Bellenger et al. (2017), has been tested against field observations made by a rising microstructure profiler during 4 rain events in the North Atlantic (ten Doeschate et al., 2019). The model demonstrated excellent agreement with observations of the subskin temperature during rain, suggesting it is accurately capturing the relevant processes occurring in the subskin layer. However, the skin layer physics have never been tested against direct observations until now.

2.2. Observations

2.2.1. Overview of Measurements

Four months of measurements of rainfall, air temperature, humidity, wind speed, radiometric skin SST, near-surface (5 cm) temperature from a towed thermistor known as a sea snake, and bulk ocean temperature and salinity were made from the R/V Revelle, stationed at the equator and 80.5 E, as part of the larger Dynamics of the Madden Julian Oscillation (DYNAMO) experiment from September to December 2011 (see e.g., Moum et al., 2014). The ship was always stationed facing westward, as both the wind and the surface current were generally eastward. Typical surface current speeds were around 0.8 m/s, while typical winds were in the range of 2–8 m/s with few observations above 10 m/s. Twin Heitronics KT15.82 8–14 µm infrared radiometers, calibrated against a blackbody in the lab, were mounted portside of the bow, one pointed at the sea surface (well outside the bow wake) and the other at the sky to enable correction for sky reflection and calculation of T_{skin} to an accuracy of $\pm 0.1°C$ (Zappa et al., 1998). Contamination of the radiometric measurement by raindrops in the optical path may introduce an additional small uncertainty at high rain rates (see Supporting Information S1 for a detailed analysis). The towed sea snake thermistor had a nominal depth of 0.05 m for this experiment, and was quality-controlled for contamination by wake effects and intermittent exposure to air, though the low relative velocity of the ship led to minimal occurrence of these issues (de Szoeke, 2021; Fairall, Bradley, Godfrey, et al., 1996). The ship intake and thermosalinograph (TSG) was located at 5 m depth; atmospheric measurements were made off the bow-mast at 16 m above the surface. The data interval was 1 min for all sensors except the radiometers, which were recording at 1 Hz.

2.2.2. Rain Event Detection

Rain events were identified algorithmically throughout the time series based on criteria from Thompson et al. (2019), who studied the occurrence of rain layers from R/V Revelle using a precipitation radar and subsurface T & S profiles during the same time period as our observations. As in Thompson et al. (2019), rain events were required to be at least 10 min in duration, and events were considered to be distinct if there were at least 30 min of no rainfall separating them. We required a minimum peak rain rate of 5 mm/hr based on the finding of Thompson et al. (2019) that a rain layer was very unlikely to form if the maximum rain rate was below this threshold, suggesting that rain effects will be difficult to discern in those cases. Finally, to account for the occasional long tails of very light rain rates measured by the shipboard sensor, we also introduced a threshold of 0.5 mm/hr below which rain rates were treated as zero. Application of these criteria led to identification of 69 separate rain events throughout the study period, comparable to the 68 events identified from the precipitation radar by Thompson et al. (2019) (see Text S2 in Supporting Information S1 for a sensitivity analysis on the event detection criteria).

Baseline values of skin temperature and other geophysical parameters of interest were calculated from the mean value during the 3 min that preceded the onset of rain, and the deviation of any given parameter from its pre-onset mean is indicated by the symbol δ. Our goal is to reference the evolution of variables to the state of the surface ocean and atmosphere immediately prior to rain, and given our 1-min data interval we feel that an average of 3 data points provides an acceptable balance between smoothing of natural variability and proximity to rain onset. Figure 2 shows an example rain event after this process was applied, along with histograms of the distribution of parameters across the 69 events.
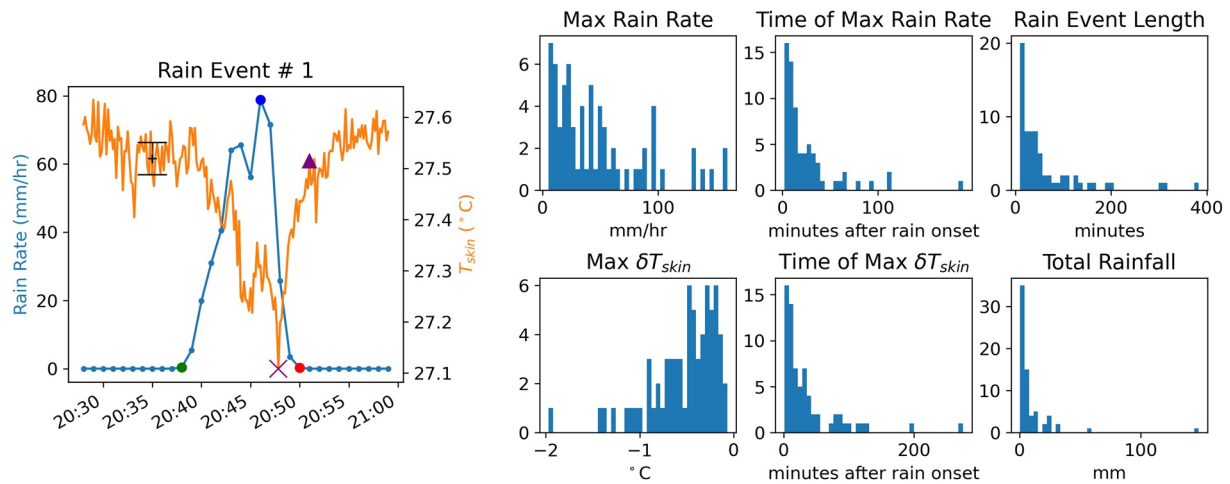
Figure 2. (left) An example rain event from the data set, showing the automated detection of key variables. Rain rate is plotted in blue, while calibrated skin temperature is plotted in orange. The automated detection algorithms provide the time of rain onset (green circle), time of max rain rate (blue circle), time of rain end (red circle), pre-onset mean skin temperature value (black error bars), time of maximum skin temperature deviation from the pre-onset mean (purple X), and time of skin temperature recovery to pre-onset mean values (purple triangle) (right) histograms of detected variables for all 69 rain events.

3. Results

3.1. Composite Timeseries

In order to generalize our observations of rainfall, skin temperature and other relevant variables in a meaningful way across 69 different rain events, we normalized the timescale of each event based on the expectation that the integral of surface heat fluxes from rain onset to the time of maximum δT_{skin} should be closely related to the magnitude of maximum δT_{skin} (in the absence of advection or large variability in subsurface turbulence). This leads to a natural scaling in terms of the time between rain onset and maximum skin temperature deviation, that is, $t_{\text{normalized}} = (t - t_{\text{onset}})/t_{\delta \text{SST}_{\text{max}}}$ where t is the original timestamp, t_{onset} denotes the onset of rain, and $t_{\delta \text{SST}_{\text{max}}}$ is the time of maximum skin temperature deviation where the term SST is used interchangeably with T_{skin} for visual simplicity. The resulting composite plots of rain rate, radiometric skin temperature, bulk sea temperature and salinity, air temperature, wind speed, specific humidity, and sensible heat flux are shown in Figure 3. The colored markers indicate the ensemble mean of all rain events at a given normalized time bin, where the gray shading spans the 10th to 90th percentile range across the events. The nature of the normalized timescale is such that all rain events are included in the bins between 0 (t_{onset}) and 1 ($t_{\delta \text{SST}_{\text{max}}}$), but only the longer events contribute to the bins at the outer edges of the composite plots. Therefore, close attention should be paid to the size of each bin marker, which reflects the number of events included in that bin, when interpreting Figure 3. For example, the sharp drop in rain rate at $t_{\text{normalized}} \cong 1.5$ is an artifact of the number of rain events in the bin, rather than being reflective of a physical process.

The time of maximum skin temperature deviation ($t_{\delta \text{SST}_{\text{max}}}$) is fairly well correlated with the time of maximum rain rate ($R^2 = 0.67$ for the 69 events), and $t_{\delta \text{SST}_{\text{max}}}$ displays even greater correlation with the overall length of the rain event ($R^2 = 0.80$). A linear fit to the composite values of rain rate versus δSST (or equivalently, δT_{skin}) between t_{onset} and $t_{\delta \text{SST}_{\text{max}}}$ yields a slope of $-0.05°$C/(mm/hr) ($R^2 = 0.95$). The mean rain rate at $t_{\delta \text{SST}_{\text{max}}}$ was 6.9 mm/hr and corresponded to a mean depression of $-0.41°$C in skin temperature. In comparison, the sea snake measured a $-0.13°$C depression in the near-surface (5 cm) temperature while the ship intake measured a $-0.03°$C depression at a depth of 5 m. The ship intake also measured a maximum salinity depression of -0.02 psu one timestep after $t_{\delta \text{SST}_{\text{max}}}$, suggestive of the delay one might expect in mixing the low-salinity signal down to 5 m depth. Air temperature decreased by an average of $-1.15°$C between rain onset and $t_{\delta \text{SST}_{\text{max}}}$, while the air-sea temperature difference $T_{\text{skin}} - T_{\text{air}}$ increased by $0.77°$C, reflecting a larger decrease in air temperature than skin temperature. Specific humidity decreased by -0.61 g/kg, while the air-sea humidity difference $q_{\text{sat}}(T_{\text{skin}}) - q_{\text{air}}$ increased only slightly, with too much variability in the signal to draw any clear conclusions. Wind speed also displayed no clear trend across the ensemble of normalized rain events, though a slight increase is visible across the period of rain onset.
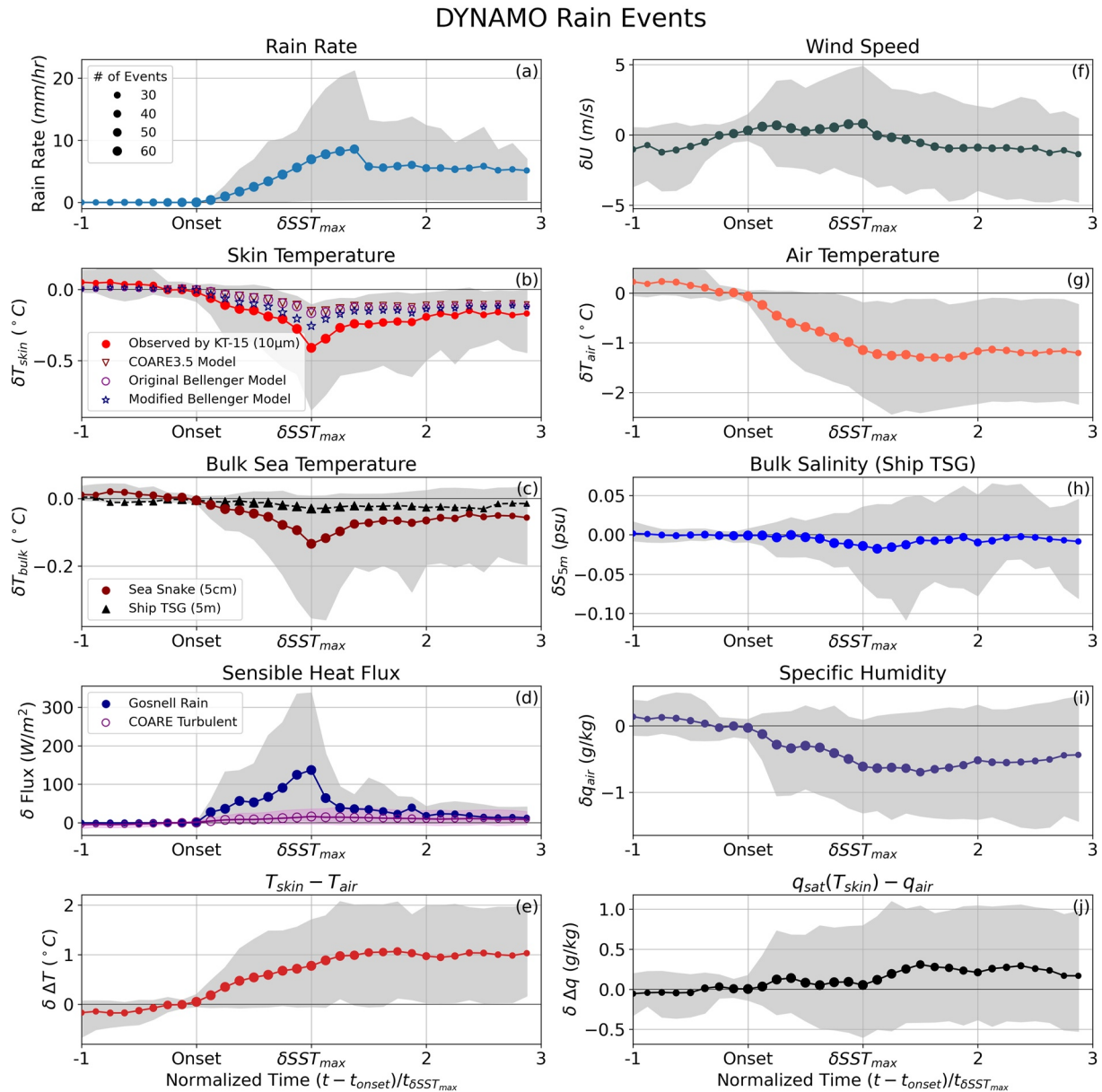
Figure 3. Composite figure showing ensemble mean changes in (a) Rain Rate, (b) Skin Temperature, (c) 5 cm and 5 m Sea Temperature, (d) Sensible Heat Flux, (e) Air-Sea Temperature Difference, (f) Wind Speed, (g) Air Temperature, (h) 5 m Salinity, (i) Specific Humidity, and (j) Air-Sea Humidity Difference across all 69 rain events, normalized by the time between rain onset and maximum skin temperature deviation. The circle sizes represent the number of rain events included in each bin, with all events included between 0 and 1 by definition of the normalized timescale. Shaded gray areas span the 10th to 90th percentile range of the rain events (shaded areas in panels (b–d) correspond to the variable plotted in filled circles). Panel (b) also displays ensemble mean modeling results discussed further in Section 3.2.

3.2. Model Evaluation

The Bellenger et al. (2017) model derived in Section 2.1 requires input of the latent, sensible, and longwave flux components that make up Q. We therefore used the COARE3.5 algorithm (Edson et al., 2013) to calculate those flux components from our observed variables prior to running the Bellenger model. As discussed in Section 2.1.1, we ran two versions of the model, the "Original" as derived in Bellenger et al. (2017), and a "Modified" version with the penetration-depth scaling coefficient $(1 − f_V(\delta))$ removed from the Gosnell et al. (1995) rain sensible heat flux Q_{Rain} and precipitation mass flux P terms in Equations 4 and 6. The ensemble mean values for the model results are shown in Figure 3b, suggesting that the Bellenger model as originally derived provides only minor improvement over the COARE3.5 algorithm, which is fully naïve to rain effects in its calculation of skin
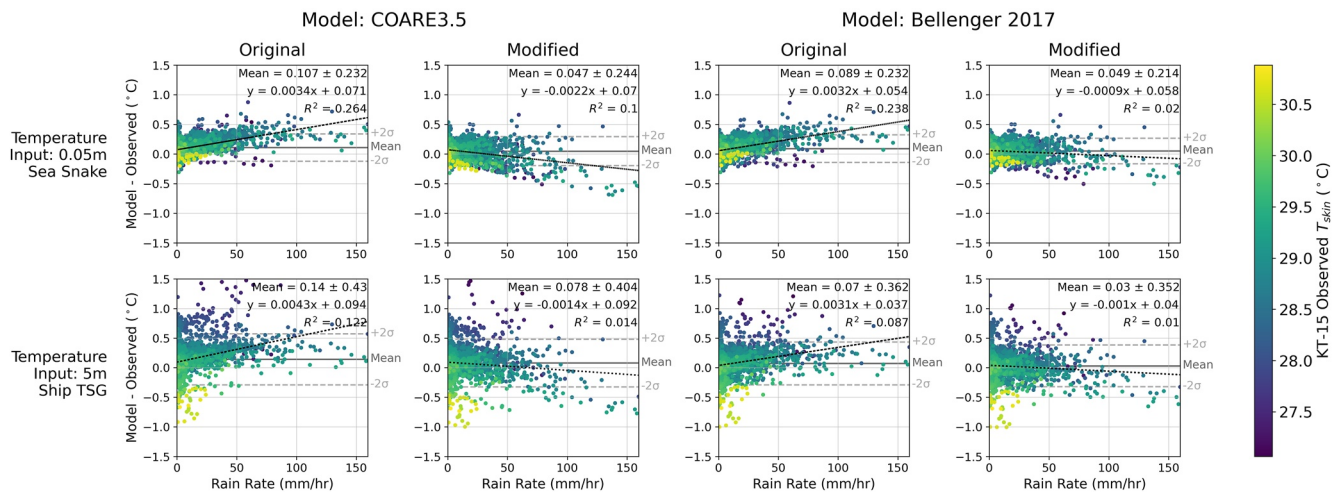
Figure 4. Modeled T_{skin}—Observed T_{skin} as a function of rain rate. Each point corresponds to a 1-min data point in one of the 69 rain events. The upper row shows model results when given the sea snake temperature as input, while the bottom shows model results when given the TSG temperature as input (all other inputs are held constant across cases). Color indicates the observed value of T_{skin}. Also shown on each plot are horizontal gray lines representing the mean of all data points ± 2 standard deviations, and a dashed black line showing a linear fit.

temperature. However, our modification to the Bellenger model further improves the agreement between modeled and observed skin temperatures in the ensemble mean, suggesting that the full volume of deposited rainwater should be taken into account when modeling rain sensible heat flux, rather than just the fraction of drops that initially penetrate to depths within the skin layer. Q_{Rain} is plotted in Figure 3d and reaches a peak ensemble mean value of 137 W/m² —the size of this term as a major fraction of the net surface heat budget suggests that it is a dominant control on skin temperature during rainfall.

Given these observations, we added a fourth modeling case by modifying the COARE3.5 algorithm to include Q_{Rain} as a term in the surface heat budget for the calculation of skin temperature. This is analogous to the implementation in the Bellenger model, but without any of the other rain effects (surface renewals, enhanced roughness, and buoyancy flux) accounted for, as the COARE3.5 algorithm calculates the skin-subskin temperature difference using the equilibrium model of Saunders (1967) as described by Fairall, Bradley, Godfrey, et al. (1996). Our "Modified COARE" is thus less physically realistic, but comparison of the Modified COARE with the Modified Bellenger provides insight as to the importance of the rain effects missing from COARE in predicting skin temperature. We ran these 4 modeling cases for every rain event with two different "bulk" temperature inputs: $T_{0.05\,m}$ from the sea snake, and $T_{5\,m}$ from the TSG. Each of these cases used the appropriate depth scaling based on the assumed temperature profile and lens depth discussed in Section 2.1. Figure 4 compares the modeled skin temperature to the observed skin temperature as a function of rain rate for every 1-min data point across all 69 rain events.

The efficacy of the modeling shown in Figure 4 is quantified by two criteria: the proximity of the difference between observed and modeled values to zero in the aggregate (both how close the mean is to zero and how big the spread is around that mean), and the linear trend with rain rate of the difference between observed and modeled values (both the slope of the linear fit and the quality of the fit should be low). These parameters, shown on Figure 4, are also summarized in Table 1. A model that is capturing the relevant rain physics effectively will have a mean difference close to zero and minimal trend with increasing rain rate. Both "Original" models display a clear trend of overestimating T_{skin} (underestimating the amount of surface cooling) with increasing rain rate, supporting the observation that the skin layer physics as originally derived by Bellenger et al. (2017) provides very minor improvement over a model without rain physics.

The "Modified" models incorporating the full Q_{Rain} term improved the proximity of the mean difference to zero by about a factor of 2 compared to the Originals in all 4 cases. Even more importantly, the Modified Bellenger model displays very little trend with rain rate, suggesting that it is representing the rain physics effectively. By contrast, the Modified COARE displays a stronger trend of underestimating T_{skin} (overestimating the amount

Table 1
Evaluation of Model Fitness for the Eight Cases Shown in Figure 4

Model name	Temperature input	Original model		Modified model		Percent improvement	
		Mean diff. (°C)	Tendency (°C/[mm/hr])	Mean diff. (°C)	Tendency (°C/[mm/hr])	Mean diff. (°C)	Tendency (°C/[mm/hr])
COARE 3.5	0.05 m (Sea Snake)	0.107 ± 0.232	0.0034 $R^2 = 0.264$	0.047 ± 0.244	-0.0022 $R^2 = 0.10$	56% (−5%)	35% (62%)
	5 m (Ship TSG)	0.140 ± 0.430	0.0043 $R^2 = 0.122$	0.078 ± 0.404	-0.0014 $R^2 = 0.01$	44% (6%)	67% (89%)
Bellenger et al. (2017)	0.05 m (Sea Snake)	0.089 ± 0.232	0.0032 $R^2 = 0.238$	0.049 ± 0.214	-0.0009 $R^2 = 0.02$	45% (8%)	72% (92%)
	5 m (Ship TSG)	0.070 ± 0.362	0.0031 $R^2 = 0.087$	0.03 ± 0.352	-0.0010 $R^2 = 0.01$	57% (3%)	68% (89%)

Note. The mean difference between observations and model output is given $\pm 2\sigma$. The tendency of the difference with increasing rain rate (the slope of a linear fit) is given along with the R^2 value for the linear fit. For each combination of model and temperature input, the percent improvement between the original model and the modified version proposed in this paper is calculated as |(Original—Modified)|/Original × 100, indicating how much closer to zero the value is for the modified model compared to the original.

of surface cooling) with increasing rain rate, demonstrating the small but not insignificant role of rain-induced turbulence and buoyancy flux in the thermal skin. At high rain rates (>50 mm/hr) where observations are relatively sparse, all of the Modified model cases are predicting too much surface cooling, which may be reflective of a change in the relevant processes at very intense rain rates (see Section 4.3 for further discussion). Finally, the aggregate performance of the models is reasonably similar when fed with temperature measurements from two very different depths, supporting the findings of ten Doeschate et al. (2019) that the Bellenger model captures the sub-skin rain physics well. However, we do see a clear trend in all of the models when using $T_{5\,m}$ of underestimation when the observed skin temperature is particularly warm, and overestimation when the observed skin temperature is particularly cold. This is likely due to advective processes occurring within the upper few meters of the ocean that the ship TSG is too deep to measure.

4. Discussion

4.1. Validity of Penetration-Depth Scaling

Our results offer strong support for the contention that it is inappropriate to scale the rain sensible heat flux in terms of the fraction of raindrops that only penetrate to within the skin layer upon initial impact. The remnants of many raindrops that initially penetrate deeper than the skin layer are likely returned toward the surface under their own buoyancy, where they may interact with other processes occurring at the subskin interface and cause buoyancy-driven surface renewals. Even penetrating drops that are mixed into the subsurface layer after impact have the potential to influence skin temperature due to the heightened levels of surface renewal being driven by the kinetic energy of subsequent raindrops.

We therefore recommend that the volume fraction scaling term $(1 - f_V(\delta))$, originally from Schlüssel et al. (1997) and shown in Figure 5, be used for determining the depth profile of raindrop-driven turbulence, but not for scaling the rain sensible heat flux. The removal of more than 80% of the rain from the heat flux calculation for rain rates above 6 mm/hr is physically unrealistic and leads to the strong tendency of the Original Bellenger model to underestimate the level of surface cooling as a function of increasing rain rate (as shown in Figure 4). In the absence of more sophisticated parameterization for the process of raindrops returning toward the surface after penetration, we have simply used the entirety of the Q_{Rain} term at all rain rates. This leads to
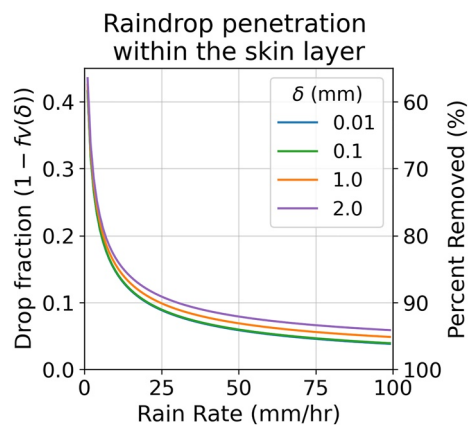
Figure 5. The raindrop penetration-depth scaling term used in the Original Bellenger model, evaluated across a range of likely rain rates and skin layer thicknesses. For ease of interpretation, the right *y*-axis displays the percentage of the total rain sensible heat flux that is removed by this term.
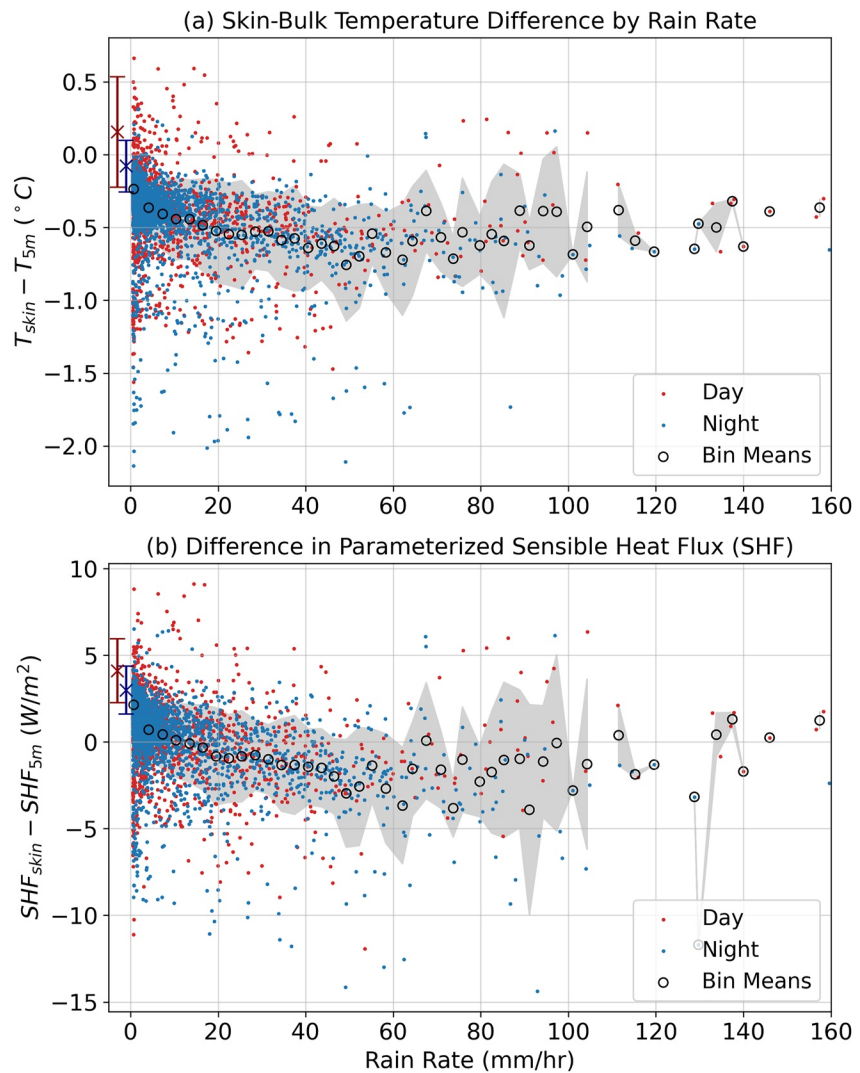
Figure 6. (a) difference between skin and 5 m ship intake ("bulk") temperature as a function of rain rate, and (b) difference in the COARE3.5 algorithm's resulting parameterization of turbulent sensible heat flux when using the two different temperature observations as inputs. Small colored dots show every 1-min data point divided into day- and night-time to visualize the potential effects of diurnal warming, open circles show bin means for 3 mm/hr rain rate bins of all data, and gray shading indicates ± 1 standard deviation. For reference, the "X" symbols with error bars at $x < 0$ show the mean and standard deviation for all day- and night-time measurements when it was not raining.

much better agreement between observations and model results, though we note that the tendency of the modified models to overestimate the surface cooling at very high rain rates may suggest a need for some additional physics in intense rains.

4.2. Secondary Effect on Turbulent Heat Flux Modeling

As shown in Figure 3c, the influence of rain on the temperature at 5 m depth is quite small, consistent with the existing body of observations that show rain effects generally being confined to the upper 3 m or so. Figure 6a shows the difference between skin temperature and 5 m ("bulk") ocean temperature as a function of rain rate, generally on the order of 0.5°C. This rain-induced vertical temperature gradient will induce a bias in current parameterizations of turbulent sensible heat fluxes if they are based on an ocean temperature measurement from below the depth of rain influence. To quantify the magnitude of this effect, we compared the sensible heat flux calculated with (Original) COARE3.5 using both temperature measurements, demonstrating that sensible heat fluxes calculated from below the depth of rain influence will be on the order of 5 W/m^2 too large (Figure 6b).

Investigating Effects of Wind Speed on Rain-Induced SST Anomalies
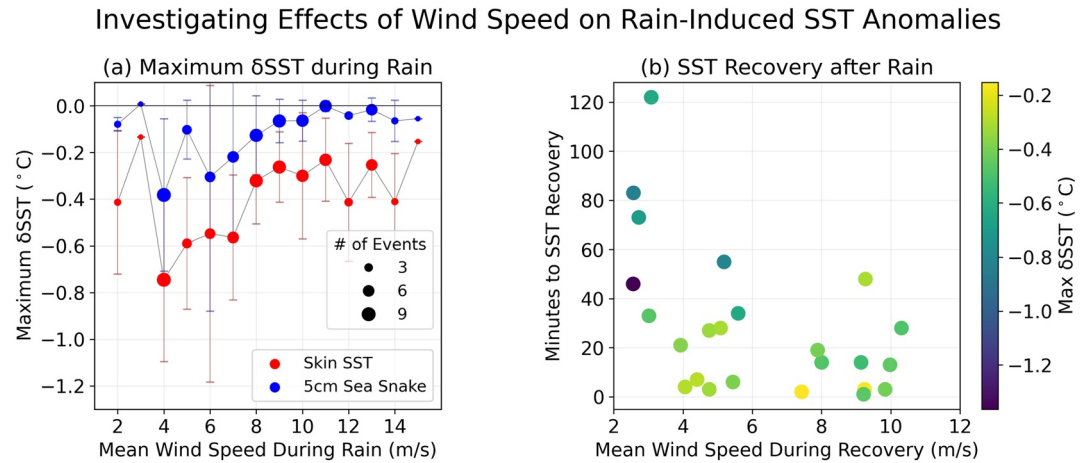
Figure 7. (a) Maximum temperature deviation during rain events as measured by both the radiometer and the sea snake, center-binned by wind speed (all events), and (b) time it took for skin temperature to return to its initial value after a rain event, plotted against mean wind speed during that time and colored by the maximum skin temperature deviation achieved during the event (selected events only).

This is a relatively small secondary effect given that the magnitude of the rain sensible heat flux is on the order of 100 W/m² at these rain rates.

4.3. Transition in Skin Layer Physics in Intense Rain

The leveling off of the skin-bulk temperature difference in Figure 6a somewhere in the 20–40 mm/hr range of rain rates is suggestive of a change in the nature of the skin layer physics such that further increases in rain rate do not correspond to further decreases in skin temperature. This is in agreement with the observations of Peirson et al. (2013), who theorized that "above a rainfall rate in the vicinity of 30 mm h⁻¹, increasing the rainfall rates may merely increase the frequency of ricocheting or spallation motions with negligible increase in deeply penetrating vertical droplet motions." At these high rain rates, the concept of a surface renewal timescale may need to be conceptually modified, as the surface is being continuously disturbed by the chaotic interaction of impinging raindrops, impact craters, upward jets, and secondary droplets. This is a likely explanation for the tendency of the Modified model to underpredict skin temperature at very high rain rates—the surface renewal physics may need to be modified. A simple alternative explanation for the observed leveling-off would be that the skin temperature quickly depresses all the way to the temperature of the rain in intense rains, so additional rainfall cannot lead to additional cooling. If this were the case, then (assuming the rain is close to the wet bulb temperature) we would expect to see the skin temperature approaching the wet bulb temperature at high rain rates; however, the skin temperature consistently remains about 4° warmer than the instantaneous wet-bulb temperature and the difference displays no trend with rain rate.

4.4. Wind Effects

Several recent observational campaigns have posited a wind threshold of 6 or 7 m/s above which the surface layer remains well-mixed in the presence of rain and no significant surface cooling or freshening is observed (Dong et al., 2017; Thompson et al., 2019; Volkov et al., 2019). However, the upper measurement depths in these campaigns ranged between 0.2 and 0.4 m, while our data set contains measurements at 0.05 m from the sea snake and skin temperature from the radiometer. Figure 7a shows the maximum temperature deviation measured by both sensors, binned by the average wind speed during each rain event. The deviation in the sea snake measurement is reasonably close to zero for wind speeds above 8 m/s, in agreement with the observations of Dong et al. (2017) and Volkov et al. (2019). However, the skin temperature depresses during all rain events regardless of wind speed. Donlon et al. (2002) presented observational evidence that the gradient across the skin layer (skin temperature—subskin temperature) approaches a constant value of −0.17°C for wind speeds above 6 m/s, and we see differences of a comparable magnitude between the skin and 5 cm temperature for winds above 6 m/s

in Figure 7a. However, we emphasize caution in using a constant value for skin temperature correction in the presence of rain given the variability in relationships between rain rate and wind speed across the oceans. This data set implies that rain will always have a non-negligible effect on skin temperature (and surface fluxes) during a rain event, and that there is no wind speed below 15 m/s (the maximum observed over a rain event in this data set) that would be appropriate as a threshold above which rain effects on the ocean skin can be neglected entirely while it is raining.

Another open question as to the influence of wind on rain-induced modulation of air-sea exchange is the persistence and evolution of the cool fresh surface layer after a rain event, which is expected to depend primarily on the level of wind-driven mixing. While Lagrangian drifter measurements would be the most appropriate data set for capturing the long-term evolution of a freshwater pool, we identified 25 events in our Eulerian data set that were characterized by one short, sharp pulse of rain with a distinct ending, minimizing (albeit not entirely removing) the role of horizontal advection in the time-evolution of the surface temperature. For these events, Figure 7b shows the relationship between the time it took for skin temperature to recover to its pre-rain value after rain stopped versus the wind speed during that recovery period. Data points are colored by the maximum δT_{skin} that occurred during the rain event.

We find that low wind speeds and large skin temperature deviation lead to skin temperature recovery timescales of 1–2 hr, while higher wind speeds correspond to smaller skin temperature deviations and quicker recovery times. This result implies that the speed of the skin layer recovery depends on the forcing, which is consistent with the finding by Zappa et al. (1998) that the restoring of the cool skin layer increases with heat flux and energy dissipation (see Figures 5 and 9 in Zappa et al., 1998). Other recent drifter observations have captured rain-induced surface anomalies persisting for timescales of up to a day at very low wind speeds (Volkov et al., 2019). Our approach is focused on events with timescales of less than an hour and limited by its Eulerian frame, and these considerations should be kept in mind when integrating our results with other studies. Also, while negative salinity and temperature anomalies in the surface ocean have been observed to be well correlated in the presence of rain (Clayson et al., 2019; Drushka et al., 2019; Flament & Sawyer, 1995), high solar insolation can warm a freshwater pool before it mixed into the underlying ocean (further reinforcing stratification), so recovery of the skin temperature should not be taken in and of itself to mean that the salinity anomaly has also recovered.

5. Conclusions

We measured the response of the surface ocean and atmosphere to 69 distinct rain events with an average peak rain rate of 6.9 mm/hr and ocean skin temperature response of −0.41°C. We found that Bellenger et al. (2017)'s model for skin temperature in the presence of rain reproduces the sub-skin physics well but tends to overestimate the skin temperature as rain rate increases. We suggest that this is due to an unrealistic scaling of the rain heat flux parameterization given by Gosnell et al. (1995) in terms of the initial penetration depth of the raindrops. Our results show that incorporation of the full (unscaled) rain heat flux term in the surface flux balance improves prediction of skin temperature at all rain rates. However, the modified model underestimates skin temperature at very high rain rates, which may be due to a transition in the relevant surface renewal physics at rain rates high enough to continuously disturb the skin. This hypothesis is supported by the observation that the skin-bulk temperature difference increases with rain rate up to a rate in the 20–40 mm/hr range, at which point it levels off, maintaining a mean value around −0.5°C with further increases in rain rate. The magnitude of the skin-bulk temperature difference during rainfall also highlights a potential bias in turbulent sensible heat fluxes parameterized from ocean temperature measurements made at depth during rain events. Failure to account for the near-surface temperature gradient induced by the rain may lead to overprediction of the turbulent sensible heat flux by around 5 W/m². Skin temperature displayed a negative response to rainfall regardless of the wind speed, while the temperature at 5 cm depth did not depress when rain events were accompanied by winds greater than 8 m/s. The largest skin temperature deviations were associated with low-wind conditions and took 1–2 hr to recover to pre-rain values, while higher winds corresponded to smaller skin temperature deviations and faster recovery times. Our results emphasize the importance of accounting for rain-induced temperature deviations in intercomparison and interpretation of in-situ and satellite data products, as well as rain-driven air-sea fluxes in modeling and prediction of weather and climate in regions of high precipitation.

Data Availability Statement

Data used in this study (Zappa et al., 2022) is archived for public access on Columbia Academic Commons (https://doi.org/10.7916/adhv-rc45).

References

Anderson, S. P., Hinton, A., & Weller, R. A. (1998). Moored observations of precipitation temperature. *Journal of Atmospheric and Oceanic Technology*, *15*(4), 979–986. https://doi.org/10.1175/1520-0426(1998)015<0979:MOOPT>2.0.CO;2

Anderson, S. P., Weller, R. A., & Lukas, R. B. (1996). Surface buoyancy forcing and the mixed layer of the Western Pacific warm pool: Observations and 1D model results. *Journal of Climate*, *9*(12), 3056–3085. https://doi.org/10.1175/1520-0442(1996)009<3056:SBFATM>2.0.CO;2

Asher, W. E., Jessup, A. T., Branch, R., & Clark, D. (2014). Observations of rain-induced near-surface salinity anomalies. *Journal of Geophysical Research: Oceans*, *119*(8), 5483–5500. https://doi.org/10.1002/2014JC009954

Bellenger, H., Drushka, K., Asher, W., Reverdin, G., Katsumata, M., & Watanabe, M. (2017). Extension of the prognostic model of sea surface temperature to rain-induced cool and fresh lenses. *Journal of Geophysical Research: Oceans*, *122*(1), 484–507. https://doi.org/10.1002/2016JC012429

Clayson, C. A., Edson, J. B., Paget, A., Graham, R., & Greenwood, B. (2019). Effects of rainfall on the atmosphere and the ocean during SPURS-2. *Oceanography*, *32*(2), 86–97. https://doi.org/10.5670/oceanog.2019.216

Craeye, C., & Schlüssel, P. (1998). Rainfall on the sea: Surface renewals and wave damping. *Boundary-Layer Meteorology*, *89*(2), 349–355. https://doi.org/10.1023/A:1001796911059

Cronin, M. F., & McPhaden, M. J. (1999). Diurnal cycle of rainfall and surface salinity in the Western Pacific Warm Pool. *Geophysical Research Letters*, *26*(23), 3465–3468. https://doi.org/10.1029/1999GL010504

de Szoeke, S. P. (2021). Fast floating temperature sensor measures SST, not wet-bulb temperature. *Journal of Atmospheric and Oceanic Technology*, *38*(5), 995–1000. https://doi.org/10.1175/JTECH-D-20-0193.1

de Szoeke, S. P., Edson, J. B., Marion, J. R., Fairall, C. W., & Bariteau, L. (2014). The MJO and air–sea interaction in TOGA COARE and DYNAMO. *Journal of Climate*, *28*(2), 597–622. https://doi.org/10.1175/JCLI-D-14-00477.1

Dong, S., Volkov, D., Goni, G., Lumpkin, R., & Foltz, G. R. (2017). Near-surface salinity and temperature structure observed with dual-sensor drifters in the subtropical South Pacific. *Journal of Geophysical Research: Oceans*, *122*(7), 5952–5969. https://doi.org/10.1002/2017JC012894

Donlon, C., Robinson, I., Casey, K. S., Vazquez-Cuervo, J., Armstrong, E., Arino, O., et al. (2007). The Global Ocean Data assimilation experiment high-resolution sea surface temperature pilot project. *Bulletin of the American Meteorological Society*, *88*(8), 1197–1214. https://doi.org/10.1175/BAMS-88-8-1197

Donlon, C. J., Minnett, P. J., Gentemann, C., Nightingale, T. J., Barton, I. J., Ward, B., & Murray, M. J. (2002). Toward improved validation of satellite sea surface skin temperature measurements for climate research. *Journal of Climate*, *15*(4), 353–369. https://doi.org/10.1175/1520-0442(2002)015<0353:TIVOSS>2.0.CO;2

Drushka, K., Asher, W. E., Jessup, A. T., Thompson, E. J., Iyer, S., & Clark, D. (2019). Capturing fresh layers with the surface salinity profiler. *Oceanography*, *32*(2), 76–85. https://doi.org/10.5670/oceanog.2019.215

Edson, J. B., & Fairall, C. W. (1994). Spray droplet modeling: 1. Lagrangian model simulation of the turbulent transport of evaporating droplets. *Journal of Geophysical Research*, *99*(C12), 25295–25311. https://doi.org/10.1029/94JC01883

Edson, J. B., Jampana, V., Weller, R. A., Bigorre, S. P., Plueddemann, A. J., Fairall, C. W., et al. (2013). On the exchange of momentum over the open ocean. *Journal of Physical Oceanography*, *43*(8), 1589–1610. https://doi.org/10.1175/JPO-D-12-0173.1

Engel, O. G. (1966). Crater depth in fluid impacts. *Journal of Applied Physics*, *37*(4), 1798–1808. https://doi.org/10.1063/1.1708605

Ewing, G., & McAlister, E. D. (1960). On the thermal boundary layer of the ocean. *Science*, *131*(3410), 1374–1376. https://doi.org/10.1126/science.131.3410.1374

Fairall, C. W., Bradley, E. F., Godfrey, J. S., Wick, G. A., Edson, J. B., & Young, G. S. (1996). Cool-skin and warm-layer effects on sea surface temperature. *Journal of Geophysical Research*, *101*(C1), 1295–1308. https://doi.org/10.1029/95JC03190

Fairall, C. W., Bradley, E. F., Rogers, D. P., Edson, J. B., & Young, G. S. (1996). Bulk parameterization of air-sea fluxes for tropical ocean-global atmosphere coupled-ocean atmosphere response experiment. *Journal of Geophysical Research*, *101*(C2), 3747–3764. https://doi.org/10.1029/95JC03205

Flament, P., & Sawyer, M. (1995). Observations of the effect of rain temperature on the surface heat flux in the intertropical convergence zone. *Journal of Physical Oceanography*, *25*(3), 413–419. https://doi.org/10.1175/1520-0485(1995)025<0413:OOTEOR>2.0.CO;2

Godfrey, J. S., Bradley, E. F., Coppin, P. A., Pender, L. F., McDougall, T. J., Schulz, E. W., & Helmond, I. (1999). Measurements of upper ocean heat and freshwater budgets near a drifting buoy in the equatorial Indian Ocean. *Journal of Geophysical Research*, *104*(C6), 13269–13302. https://doi.org/10.1029/1999JC900045

Gosnell, R., Fairall, C. W., & Webster, P. J. (1995). The sensible heat of rainfall in the tropical ocean. *Journal of Geophysical Research*, *100*(C9), 18437–18442. https://doi.org/10.1029/95JC01833

Harrison, E. L., & Veron, F. (2017). Near-surface turbulence and buoyancy induced by heavy rainfall. *Journal of Fluid Mechanics*, *830*, 602–630. https://doi.org/10.1017/jfm.2017.602

Houk, D., & Green, T. (1976). A note on surface waves due to rain. *Journal of Geophysical Research*, *81*(24), 4482–4484. https://doi.org/10.1029/JC081i024p04482

Jessup, A. T., Zappa, C. J., Loewen, M. R., & Hesany, V. (1997). Infrared remote sensing of breaking waves. *Nature*, *385*(6611), 52–55. Article 6611. https://doi.org/10.1038/385052a0

Katsaros, K. (1980). Radiative sensing of sea surface temperature. In F. Dobson, L. Hasse, & R. Davis (Eds.), *Air-sea interaction* (pp. 293–317). Springer US. https://doi.org/10.1007/978-1-4615-9182-5_17

Kudryavtsev, V. N., & Soloviev, A. V. (1990). Slippery near-surface layer of the ocean arising due to daytime solar heating. *Journal of Physical Oceanography*, *20*(5), 617–628. https://doi.org/10.1175/1520-0485(1990)020<0617:SNSLOT>2.0.CO;2

Laxague, N. J. M., & Zappa, C. J. (2020). The impact of rain on ocean surface waves and currents. *Geophysical Research Letters*, *47*(7), e2020GL087287. https://doi.org/10.1029/2020GL087287

Li, Y., & Carbone, R. E. (2012). Excitation of rainfall over the tropical Western Pacific. *Journal of the Atmospheric Sciences*, *69*(10), 2983–2994. https://doi.org/10.1175/JAS-D-11-0245.1

Lukas, R., & Lindstrom, E. (1991). The mixed layer of the Western equatorial Pacific Ocean. *Journal of Geophysical Research*, *96*(S01), 3343–3357. https://doi.org/10.1029/90JC01951

Marshall, J. S., & Palmer, W. M. K. (1948). The distribution of raindrops with size. *Journal of the Atmospheric Science*s, 5(4), 165–166. https://doi.org/10.1175/1520-0469(1948)005<0165:TDORWS>2.0.CO;2

Morton, D., Rudman, M., & Jong-Leng, L. (2000). An investigation of the flow regimes resulting from splashing drops. *Physics of Fluids*, *12*(4), 747–763. https://doi.org/10.1063/1.870332

Moum, J. N., de Szoeke, S. P., Smyth, W. D., Edson, J. B., DeWitt, H. L., Moulin, A. J., et al. (2014). Air–Sea interactions from westerly wind bursts during the November 2011 MJO in the Indian Ocean. *Bulletin of the American Meteorological Society*, *95*(8), 1185–1199. https://doi.org/10.1175/BAMS-D-12-00225.1

Mueller, J. A., & Veron, F. (2014). Impact of sea spray on air–sea fluxes. Part I: Results from stochastic simulations of sea spray drops over the ocean. *Journal of Physical Oceanography*, *44*(11), 2817–2834. https://doi.org/10.1175/JPO-D-13-0245.1

Oğuz, H. N., & Prosperetti, A. (1991). Numerical calculation of the underwater noise of rain. *Journal of Fluid Mechanic*s, *228*, 417–442. https://doi.org/10.1017/S0022112091002768

Peirson, W. L., Beyá, J. F., Banner, M. L., Peral, J. S., & Azarmsa, S. A. (2013). Rain-induced attenuation of deep-water waves. *Journal of Fluid Mechanics*, *724*, 5–35. https://doi.org/10.1017/jfm.2013.87

Poon, Y.-K., Tang, S., & Wu, J. (1992). Interactions between rain and wind waves. *Journal of Physical Oceanography*, *22*(9), 976–987. https://doi.org/10.1175/1520-0485(1992)022<0976:IBRAWW>2.0.CO;2

Prosperetti, A., & Oguz, H. N. (1993). The impact of drops on liquid surfaces and the underwater noise of rain. *Annual Review of Fluid Mechanics*, *25*(1), 577–602. https://doi.org/10.1146/annurev.fl.25.010193.003045

Reverdin, G., Morisset, S., Boutin, J., & Martin, N. (2012). Rain-induced variability of near sea-surface T and S from drifter data. *Journal of Geophysical Research*, *117*(C2). https://doi.org/10.1029/2011JC007549

Reverdin, G., Supply, A., Drushka, K., Thompson, E. J., Asher, W. E., & Lourenço, A. (2020). Intense and small freshwater pools from rainfall investigated during spurs-2 on 9 November 2017 in the eastern tropical Pacific. *Journal of Geophysical Research: Oceans*, *125*(2), e2019JC015558. https://doi.org/10.1029/2019JC015558

Saunders, P. M. (1967). The temperature at the ocean-air interface. *Journal of the Atmospheric Sciences*, *24*(3), 269–273. https://doi.org/10.1175/1520-0469(1967)024<0269:TTATOA>2.0.CO;2

Schlüssel, P., Soloviev, A. V., & Emery, W. J. (1997). Cool and freshwater skin of the ocean during rainfall. *Boundary-Layer Meteorology*, *82*(3), 439–474. https://doi.org/10.1023/A:1000225700380

Shcherbina, A., D'Asaro, E., & Harcourt, R. (2019). Rain and Sun create slippery layers in the eastern Pacific fresh pool. *Oceanography*, *32*(2), 98–107. https://doi.org/10.5670/oceanog.2019.217

Smyth, W. D., Hebert, D., & Moum, J. N. (1996a). Local ocean response to a multiphase westerly wind burst: 1. Dynamic response. *Journal of Geophysical Research*, *101*(C10), 22495–22512. https://doi.org/10.1029/96JC02005

Smyth, W. D., Hebert, D., & Moum, J. N. (1996b). Local ocean response to a multiphase westerly wind burst: 2. Thermal and freshwater responses. *Journal of Geophysical Research*, *101*(C10), 22513–22533. https://doi.org/10.1029/96JC02006

Smyth, W. D., Zavialov, P. O., & Moum, J. N. (1997). Decay of turbulence in the upper ocean following sudden isolation from surface forcing. *Journal of Physical Oceanography*, *27*(5), 810–822. https://doi.org/10.1175/1520-0485(1997)027<0810:DOTITU>2.0.CO;2

Soloviev, A., & Lukas, R. (1996). Observation of spatial variability of diurnal thermocline and rain-formed Halocline in the Western Pacific warm pool. *Journal of Physical Oceanography*, *26*(11), 2529–2538. https://doi.org/10.1175/1520-0485(1996)026<2529:OOSVOD>2.0.CO;2

Soloviev, A., & Lukas, R. (1997a). Observation of large diurnal warming events in the near-surface layer of the Western equatorial Pacific warm pool. *Deep Sea Research Part I: Oceanographic Research Papers*, *44*(6), 1055–1076. https://doi.org/10.1016/S0967-0637(96)00124-0

Soloviev, A., & Lukas, R. (1997b). Sharp frontal interfaces in the near-surface layer of the ocean in the Western equatorial Pacific warm pool. *Journal of Physical Oceanography*, *27*(6), 999–1017. https://doi.org/10.1175/1520-0485(1997)027<0999:SFIITN>2.0.CO;2

Soloviev, A., Lukas, R., & Matsuura, H. (2002). Sharp frontal interfaces in the near-surface layer of the tropical ocean. *Journal of Marine Systems*, *37*(1), 47–68. https://doi.org/10.1016/S0924-7963(02)00195-1

Soloviev, A., Matt, S., & Fujimara, A. (2015). Three-dimensional Dynamics of freshwater lenses in the oceanocean's near-surface layer. *Oceanography*, *28*(1), 142–149. https://doi.org/10.5670/oceanog.2015.14

Soloviev, A. V., & Schlüssel, P. (1996). Evolution of cool skin and direct air-sea gas transfer coefficient during daytime. *Boundary-Layer Meteorology*, *77*(1), 45–68. https://doi.org/10.1007/BF00121858

Takaya, Y., Bidlot, J.-R., Beljaars, A. C. M., & Janssen, P. A. E. M. (2010). Refinements to a prognostic scheme of skin sea surface temperature. *Journal of Geophysical Research: Oceans*, *115*(C6), C06009. https://doi.org/10.1029/2009JC005985

ten Doeschate, A., Sutherland, G., Bellenger, H., Landwehr, S., Esters, L., & Ward, B. (2019). Upper ocean response to rain observed from a vertical profiler. *Journal of Geophysical Research: Oceans*, *124*(6), 3664–3681. https://doi.org/10.1029/2018JC014060

Thompson, E. J., Moum, J. N., Fairall, C. W., & Rutledge, S. A. (2019). Wind limits on rain layers and diurnal warm layers. *Journal of Geophysical Research: Oceans*, *124*(2), 897–924. https://doi.org/10.1029/2018JC014130

Veron, F. (2015). Ocean spray. *Annual Review of Fluid Mechanic*s, *47*(1), 507–538. https://doi.org/10.1146/annurev-fluid-010814-014651

Volkov, D., Dong, S., Foltz, G., Goni, G., & Lumpkin, R. (2019). Observations of near-surface salinity and temperature structure with dual-sensor Lagrangian drifters during SPURS-2. *Oceanography*, *32*(2), 66–75. https://doi.org/10.5670/oceanog.2019.214

Wijesekera, H. W., Paulson, C. A., & Huyer, A. (1999). The effect of rainfall on the surface layer during a westerly wind burst in the Western equatorial Pacific. *Journal of Physical Oceanography*, *29*(4), 612–632. https://doi.org/10.1175/1520-0485(1999)029<0612:TEOROT>2.0.CO;2

Wijesekera, H. W., & Gregg, M. C. (1996). Surface layer response to weak winds, westerly bursts, and rain squalls in the Western Pacific warm pool. *Journal of Geophysical Research*, *101*(C1), 977–997. https://doi.org/10.1029/95JC02553

Wijesekera, H. W., Paulson, C. A., & Skyllingstad, E. D. (2003). Modeling the evolution of a fresh sea surface anomaly produced by tropical rainfall. *Journal of Geophysical Research*, *108*(C11), 3338. https://doi.org/10.1029/2002JC001408

Wurl, O., Landing, W. M., Mustaffa, N. I. H., Ribas-Ribas, M., Witte, C. R., & Zappa, C. J. (2018). The Ocean's skin layer in the tropics. *Journal of Geophysical Research: Oceans*, *124*(1), 59–74. https://doi.org/10.1029/2018JC014021

You, Y. (1995). Salinity variability and its role in the barrier-layer formation during TOGA-COARE. *Journal of Physical Oceanography*, *25*(11), 2778–2807. https://doi.org/10.1175/1520-0485(1995)025<2778:SVAIRI>2.0.CO;2

Zappa, C. J., Banner, M. L., Schultz, H., Corrada-Emmanuel, A., Wolff, L. B., & Jacob, Y. (2008). Retrieval of short ocean wave slope using polarimetric imaging. *Measurement Science and Technology*, *19*(5), 055503. https://doi.org/10.1088/0957-0233/19/5/055503

Zappa, C. J., Ho, D. T., McGillis, W. R., Banner, M. L., Dacey, J. W. H., Bliven, L. F., et al. (2009). Rain-induced turbulence and air-sea gas transfer. *Journal of Geophysical Research*, *114*(C7), C07009. https://doi.org/10.1029/2008JC005008

Zappa, C. J., Jessup, A. T., & Yeh, H. (1998). Skin layer recovery of free-surface wakes: Relationship to surface renewal and dependence on heat flux and background turbulence. *Journal of Geophysical Research*, *103*(C10), 21711–21722. https://doi.org/10.1029/98JC01942

Zappa, C. J., Witte, C. R., & Edson, J. B. (2022). Data for: The response of Ocean Skin temperature to rain: Observations and Implications for parameterization of rain-induced fluxes (version 1) [Dataset]. Columbia Academic Commons. https://doi.org/10.7916/adhv-rc45

Zeng, X., & Beljaars, A. (2005). A prognostic scheme of sea surface skin temperature for modeling and data assimilation. *Geophysical Research Letters*, *32*(14). https://doi.org/10.1029/2005GL023030